

# **CFD modelling of a small-scale fixed multi-chamber OWC device**

**Mohammad Shalby<sup>1,2,\*</sup>, Ahmed Elhanafi<sup>3</sup>, Paul Walker<sup>1</sup> and David G. Dorrell<sup>4</sup>**

<sup>1</sup> School of Mechanical, and Mechatronic Systems, University of Technology Sydney, Sydney, NSW 2007, Australia.

<sup>2</sup> Faculty of Engineering, Department of Mechanical Engineering, Al-Hussein Bin Talal University, Ma'an, Jordan.

<sup>3</sup> National Centre for Maritime Engineering and Hydrodynamics, Australian Maritime College, University of Tasmania, Launceston, Tasmania 7250, Australia.

<sup>4</sup> School of Engineering, Howard College Campus, University of KwaZulu-Natal, Durban 4041, South Africa.

## **Abstract**

Wave Energy Converters (WECs) have excellent potential as a source of renewable energy that is yet to be commercially realised. Recent attention has focused on the installation of Oscillating Water Column (OWC) devices as a part of harbor walls to provide advantages of cost-sharing structures and proximity of power generation facilities to existing infrastructure. In this paper, an incompressible three-dimensional CFD model is constructed to simulate a fixed Multi-Chamber OWC (MC-OWC) device. The CFD model is validated; the simulation results are found to be in good agreement with experimental results obtained from a scale physical model tested in a wave tank. The validated CFD model is then used for a benchmark study of 96 numerical tests. These investigate the effects of the PTO damping caused by the power take-off (PTO) system on device performance. The performance is assessed for a range of regular wave heights and periods. The results demonstrate that a PTO system with an intermediate damping can be used for all chambers in the MC-OWC device for most wave period ranges, except for the long wave periods. These require a higher PTO damping. An increased incident wave height reduces the device capture width ratio, but there is a noticeable improvement for long wave periods.

**Keywords:** Wave Energy; Oscillating Water Column; Multi-Chamber OWC; CFD; Experiments

---

Corresponding author: Mohammad Shalby.

E-mail: [Mohammad.shalby@student.uts.edu.au](mailto:Mohammad.shalby@student.uts.edu.au)

## Nomenclature

$A_1$	Chamber area	(m <sup>2</sup> )
$A_2$	Orifice opening area	(m <sup>2</sup> )
$b$	width of the device	(m)
$C_d$	Coefficient of discharge	(–)
$Di$	Orifice diameter	(m)
$d$	The device draught	(m)
$Gi$	Wave gauge number ( $i=1,2,3$ and 4)	(–)
$H$	Wave height	(m)
$h$	Water depth	(m)
$k$	Wavenumber	(m <sup>-1</sup> )
$g$	The gravitational acceleration	(m s <sup>-2</sup> )
$L$	Wave length	(m)
$L_C$	Chamber length	(m)
$N$	Number of the values	(–)
$P_{in}$	Mean incident power per meter of the wave crest	(W m <sup>-1</sup> )
$P_{atm}$	Atmospheric air pressure at standard temperature and pressure	(Pa)
$\Delta P$	Differential air pressure ( $P_{in} - P_{atm}$ )	(Pa)
$\bar{p}$	The fluid mean pressure field	(Pa)
$Q$	Airflow rate	(m <sup>3</sup> s <sup>-1</sup> )
$R$	Correlation coefficient	(–)
$Ri$	Opening ratio	(–)
$Re$	The Reynolds number	(–)
$t$	Time	(s)
$\Delta t$	Time step	(s)
$Ti$	Wave period	(s)
$T_R$	Resonant period	(s)
$V(t)$	The induced voltage	(V)
$w$	The vertical component of air velocity	(m s <sup>-1</sup> )
$d\eta/dt$	The free surface vertical velocity	(m s <sup>-1</sup> )
$\bar{u}$	The fluid mean velocity field	(m s <sup>-1</sup> )
$X_{max}$	The maximum values of the data from the laboratory tests	(–)
$X_{min}$	The minimum values of the data from the laboratory tests	(–)
$x_i$	The experimental data	(–)
$y_i$	The corresponding numerical data	(–)
$\Delta x$	Mesh cell size in the longitudinal direction	(m)
$\Delta z$	Mesh cell size in the vertical direction	(m)
$\alpha$	Calibration constant	(–)
$\tau$	PTO damping coefficient	(kg <sup>1/2</sup> m <sup>-7/2</sup> )
$\tau_{max}$	The maximum value of the PTO damping coefficient	(kg <sup>1/2</sup> m <sup>-7/2</sup> )
$\tau_{min}$	The minimum value of the PTO damping coefficient	(kg <sup>1/2</sup> m <sup>-7/2</sup> )
$\rho_{air}$	Air density (=1.2 for dry air at 293 K)	(kg m <sup>-3</sup> )
$\rho_w$	Water density (= 998.2 at 293 K )	(kg m <sup>-3</sup> )

$\eta$	Water surface elevation	(m)
$\varepsilon$	Capture width ratio	(–)
$\varepsilon_{total}$	The overall capture width ratio	(–)
$\omega$	Angular frequency	(s <sup>-1</sup> )
$\omega_R$	Resonant angular frequency	(s <sup>-1</sup> )
$\tau_{ij}$	The viscous stress tensor	(Pa)

## 1. Introduction

There is a growing interest around the world in the utilisation of wave energy for electricity generation. This is because wave energy is considered to be more predictable than wind and solar energy, and it has a relatively high power density compared to solar and wind power, which allows the extraction of more energy in a smaller area [1]. For coastal regions or some remote islands, wave energy is a promising renewable power source due to its high predictability. Recently, a number of prototypes for different Wave Energy Converters (WECs) have been developed around the world to meet renewable energy targets [2]; however, commercial exploitation of WECs is still limited.

At present, most of the technologies for wave energy extraction are still at the infancy stage of development, and there is a very limited number of WEC devices that are suitable for the commercial pilot demonstration stage, especially in countries with extensive coastlines, such as Australia, Denmark, Ireland, Portugal, U.K., and the U.S.A. [3-5]. The design and development of WECs is a complicated, long-term (starting from scientific first principles, then proof-of-concept prototypes and forward to the commercialization stage) and expensive process [2, 6, 7]. During this process, there are multiple areas that need to be studied and analysed to help develop these technologies and the associated project deployment. There is no single method of assessment of WEC development and performance, but the Technology Readiness Level (TRL) can be considered as a standard indicator for the advancement in the design and construction of a WEC [8].

The Oscillating Water Column (OWC) device is considered as one of the most successful technologies for harvesting ocean wave energy [9, 10]. This device was initially studied in the 1940s by Yoshio Masuda who developed a navigation buoy powered by an OWC device [11]. The OWC device can be a shoreline-based structure, such as the Portuguese Pico plant [12] or be combined with a breakwater, such as at Sakata Harbour, Japan [13]. The device can be near-shore and an ocean-bed-standing structure, such as the PK1 prototype which

was developed by Oceanlinx Ltd in Australia and tested in 2005 [14], or on a floating platform such as the Mighty Whale as developed in Japan [15]. The main aim of the future development phases of WECs is the installation of multiple devices in array configurations, which is expected to increase, in a more economical way, the amount of wave energy extracted [16, 17].

Most previous research focused on onshore and offshore isolated OWC devices with only one chamber. The optimum performance of these devices is usually obtained at the chamber resonant period [11]. Thus, there are very limited studies on the concept and performance of multi-chamber OWC (MC-OWC) devices. An extensive review of these studies can be found in [18]. The Seabreath is considered as an example of a floating multi-chamber OWC device that has been under development at Padova University, Italy since 2008 [19, 20], however, limited research has been published on this device. For instance, Martinelli et al. [19] built a lumped model to simulate the airflow inside the pipes of the Seabreath device, which was then used to assess the device efficiency based on the Italian sea environment. Another multi-chamber OWC system is the LEANCON, which is arranged in two rows in a V-shaped formation. The hydraulic mechanism of the LEANCON model was designed by Rasmussen [21] and tested at Aalborg University in Denmark [22]. A similar MC-OWC device consisting of a large floating structure made of two legs forming a V-configuration at a 90-degree with 32 chambers was physically and numerically tested at the University College Cork, Ireland [23].

The MC-OWC devices have the advantage of being suitable for deployment at shoreline locations such as a harbour wall, or wharf [11, 18]. This advantage leads to the benefits of community cost sharing and onshore power system connection with potentially high economic viability for a fully developed system. However, shoreline locations, compared to offshore sites, are subjected to waves with reduced energy content which limits the potential deployment of large numbers of devices [24]. Some studies were carried out to assess the feasibility of WECs performance in low energetic locations (near shoreline) [25, 26]. These studies revealed that integrating OWC devices into a structure in a near shoreline location (i.e., breakwater or harbour) is a potentially viable investment that could contribute towards making WECs more competitive with other renewable energy devices [27].

New South Wales (NSW), Australia, has coastal towns and cities that have many ports and jetties which could be good locations for WEC and deployment. Therefore, a MC-OWC scale device with four chambers was built in the University of Technology Sydney; this was

aimed at a long-term research project. The design of this device was based on several years of research. For example, Dorrell et al. [28] tested the first design of three chambers OWC device at the University of Glasgow in 2003 and then performed initial verification of the model concept [29, 30] followed by a series of studies to develop a mathematical model that describes the hydrodynamic performance of two and three chamber OWC devices [45-49]. In 2012, Hsieh et al. [31] built and tested a wave tank scale model of a side-mounted OWC device consisting of two chambers equipped with two Savonius turbines. Three years later, the initial testing of a new configuration based on a four chamber OWC device concept was carried out under regular wave conditions [32]. Recently, Shalby et al. [33] developed a time domain model using the rigid piston approach to define the internal chamber free surface elevation and differential chamber air pressure.

Although the above-mentioned research on MC-OWC devices delivered a good understanding of device performance, the effects of power take-off (PTO) damping on the free surface elevation inside the chamber, air pressure, airflow rate and device capture width ratio under different incident wave conditions have not yet been investigated. Therefore, this paper contributes to the existing knowledge by addressing omissions in previous work by putting forward detailed explanations of the effect of PTO damping on MC-OWC device performance using a well-validated 3D CFD model. To date, all previous numerical modelling of MC-OWC devices (two, three and four chambers) was performed using potential flow solvers which provides insights and important information at relatively low computation costs. However, these solvers are not capable of modelling the mutual coupling between the water and air flow in the chambers, non-linearity, real fluid effects due to viscosity, turbulence, and vortex shedding that may impact the performance of OWC devices [34]. To address these shortcomings, Computational Fluid Dynamics (CFD) solvers are an excellent tool for modelling MC-OWC devices. In recent years, several researchers have used CFD to simulate OWCs – these have only one chamber, and the studies were done for a variety of reasons. For a comprehensive review on modelling OWC devices in CFD reference should be made to [35]. To the best of the authors' knowledge, no previous CFD work tested the applicability of CFD for modelling a MC-OWC device, except Elhanafi et al. [36]. They recently developed and used, without experimental validations, 2D and 3D CFD simulations to compare the performance of single-chamber and double-chamber OWC devices. Therefore, constructing and experimentally validating a CFD model for a MC-OWC device of four chambers is considered as the second contribution of this paper.

In this paper, physical scale model experiments of a MC–OWC are performed and used to verify a 3D CFD model. This uses Reynolds Averaged Navier–Stokes (RANS) equations and a Volume of Fluid (VOF) surface capture strategy (RANS–VOF). With this verification, the CFD model was used for the study of the effects of PTO damping on device performance under different incident wave conditions.

## 2. Experiment setup

Regular wave tests are essential during the early stage of a WEC development program. These tests are limited and conducted for verifying the concept of a device, validating and calibrating mathematical models [6]. In this paper, regular wave conditions were utilized to validate a 3D CFD model of a MC–OWC device.

### 2.1. Physical model and testing facility

A 1:25 scale physical model is considered in this study. This is shown in Fig. 1. The model consists of four aligned rectangular chambers (each of 150 mm × 365 mm) with open bottoms and asymmetric front and rear lips. The device was designed to be aligned perpendicular to the incident wave crests (see Fig. 2). In terms of the standard classification of WECs, the proposed device could be categorized as a fixed OWC device. The design used here has simple device geometry which uses a similar design concept proposed in [19]. The device is small-scale and was constructed of 10 mm Perspex, and the internal length, width and height of the OWC chamber are shown in Fig. 1 (a). This figure also shows that the model was mounted on the flume side walls by two horizontal rectangular sections, which were locked to the flume side walls using clamps (see Fig. 1 (a)).

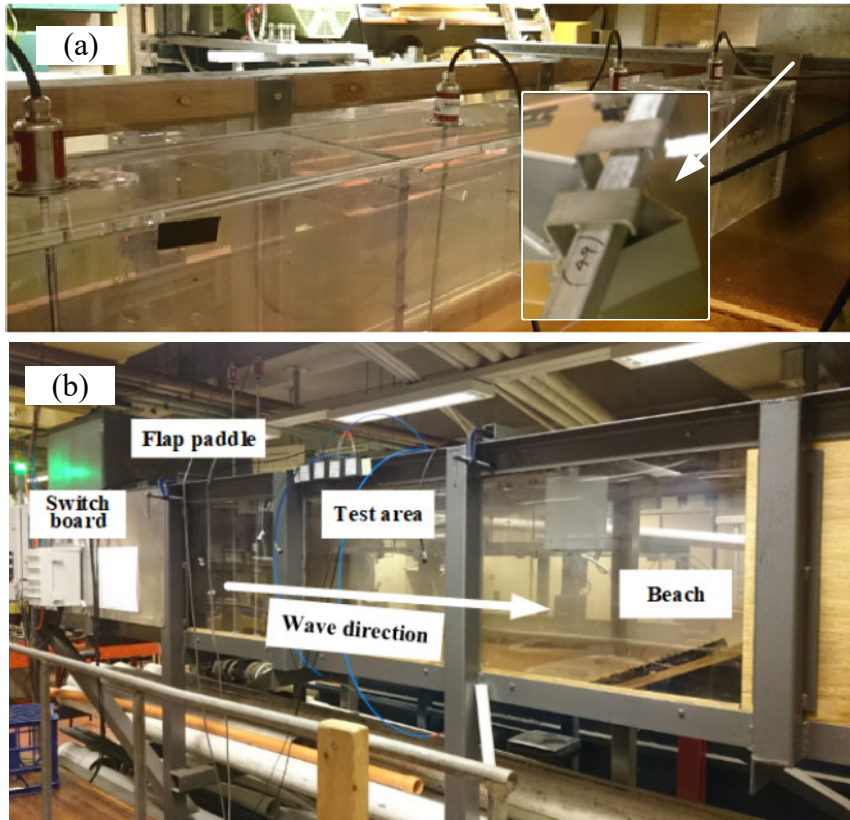


Fig. 1. Physical scale model MC–OWC device tested in the present study

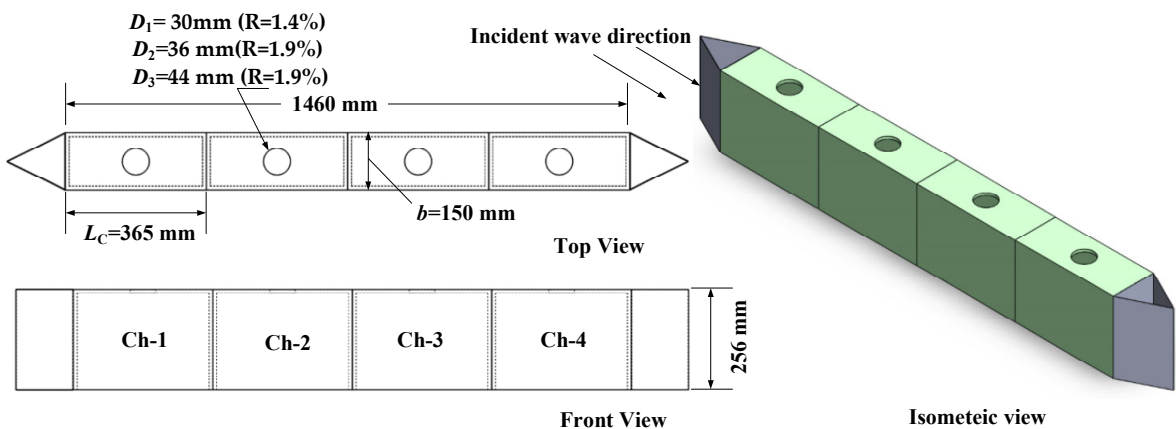


Fig. 2. MC–OWC model geometry

The scale device was tested in the wave tank of the Renewable Energy Lab at the University of Technology Sydney (UTS). The wave tank had a hydraulic paddle at one end for wave generation as shown in Fig. 1 (b). The wavemaker can only generate limited regular wave conditions. The waves from controlled paddle travel about twice the length of the paddle depth (0.5 m) before settling, thus the generated waves become fully developed in the test section which starts at a distance of 1.3 m from the paddle as shown in Fig. 3 [37]. The test section of the wave tank was 4.3 m long and 0.9 m wide. The ratio between the tank width (0.9 m) and the physical model width ( $b = 0.15$  m) is 6.0, which is more than the minimum ratio requirement of 5.0 defined in [38]; hence the tank sidewall effect can be

neglected in this study. The depth of the water in the tank was set as 0.5 m which represents 12 m at full scale. The water depth in the wave tank was kept constant during the test through the water circulation system (see the front view in Fig.3). This system works to reduce the wave reflection alongside the inclined over-topping beach (sloped at 1:4) which is covered with an absorbent layer of foam at the end of the wave tank. The reflection coefficient was found to be less than 2 % in the range of wavelengths tested, which met the standard characteristic of an absorbing beach mentioned in [39]. The sampling rate of the data acquisition system was 10 Hz and the data collection time period was limited to 20-s to avoid any re-reflection of waves from the wavemaker. Fig. 3 shows the MC-OWC system in the flume along with the locations of the wave probes and pressure sensors.

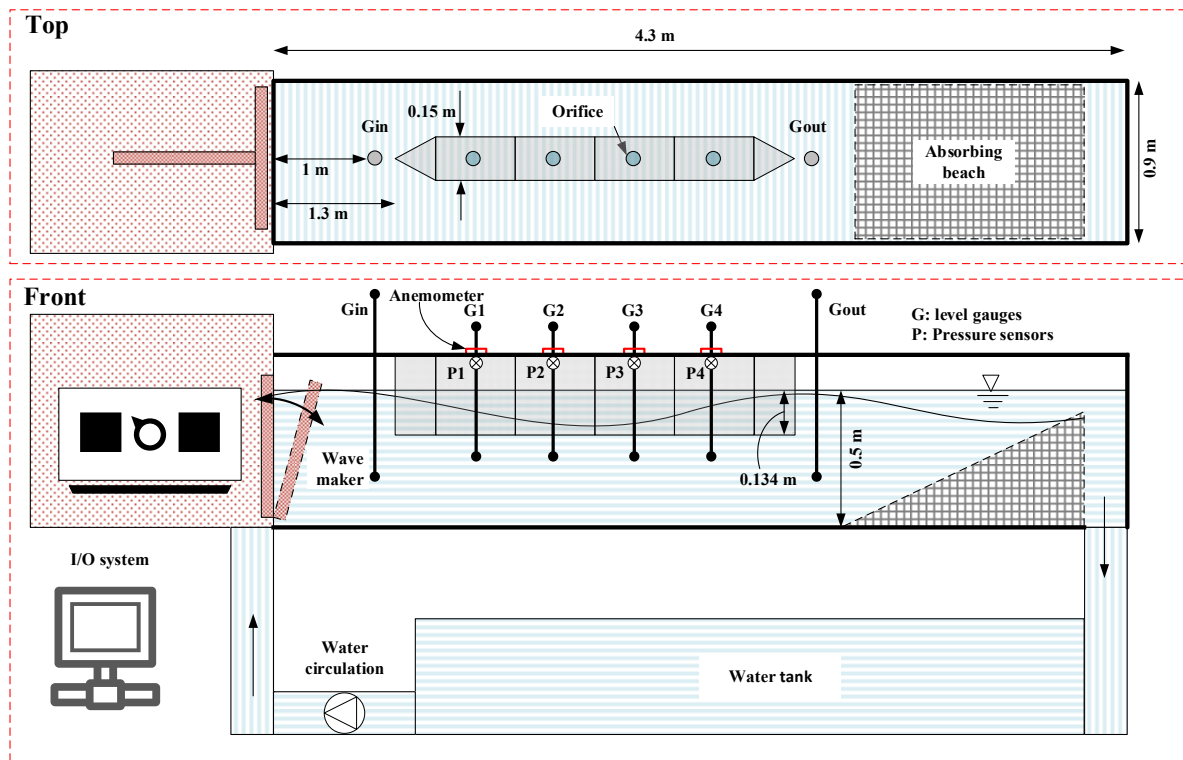


Fig. 3. The experimental setup configuration

## 2.2. Modelling the PTO system

Not all components in the energy conversion chain, from wave-to-wire, of a WEC, can be scaled accurately [6, 40]. This includes the losses in each energy conversion stage and possibly the PTO system. PTO systems can be rather simple, or they can have very advanced configurations which can be modelled successfully by modifying the mathematical model of the energy extraction mechanism to introduce nonlinearities.

Generally, the PTO system can be represented in a simplified way by an orifice (to simulate a nonlinear PTO representing an impulse turbine) [41-45] or a porous material (to

simulate a linear PTO representing a Wells turbine) [46, 47]. In this work, the PTO damping depends on the orifice diameter of the physical test, but in reality, it depends on the turbine diameter and rotational speed [48]. Orifice plates of different diameters ( $D_i$ ) were used as shown in Fig. 2. They were constructed using 3D printing and attached to the centre of each chamber top plate. Each orifice was represented by its diameter ( $D_i$ ) and the opening ratio ( $R_i$ ). The opening ratio is defined as the ratio between the orifice area and the chamber waterplane area ( $L_c \times b$ ) in percentage %.

A relationship between the pressure difference ( $\Delta P = P_{in} - P_{atm}$ ) and the airflow rate ( $Q$ ) through the orifice is given by Eq.(1) as defined in [48]

$$\tau = \sqrt{\Delta P} / Q \quad (1)$$

This relationship is quantified here for each orifice by means of the PTO damping coefficient ( $\tau$ ), which has been shown to have a significant effect on OWC performance [49]. This has almost a quadratic relationship with constant damping (constant orifice diameter), as proven by López et al. (2014) and Simonetti et al. (2015) [50, 51].

For steady flow, the relationship between the pressure change  $\Delta P$  (in Pascals) and the air flow rate across the orifice  $Q$  (in  $m^3/s$ ), was determined by using the standard orifice theory given by

$$Q = C_d A_2 \sqrt{\frac{2 |\Delta P|}{\rho_{air}}} \quad (2)$$

where  $C_d$  is the discharge coefficient that was pre-calibrated and found to be 0.55,  $A_2$  is the circular orifice area, and  $\rho_{air}$  is the air density (1.2 kg/m<sup>3</sup> for dry air at 293 K).

### 2.3. Instrumentation

The free surface elevation ( $\eta$ ) inside each chamber was measured at the centre of the chamber (i.e., at  $L_c/2$  and  $b/2$ ) using wave gauges G1–G4 (model: C-Series Core Sensor, CS). Each wave gauge comprised of a magnetic float level transmitter 5 mm in diameter with a stroke length of 250 mm. The sampling rate of the data collection was also 500 Hz. The induced voltage  $V(t)$  was digitized at 1500 Hz (0.6 m.s period) and the free-surface displacement was calculated from the relation  $\eta(t) = \alpha \times V(t)$  where the coefficient  $\alpha$  was obtained through the static calibration of each wave gauge. The differential air pressure was measured in the chamber ( $\Delta P$ ), four differential pressure transmitters P1–P4 (model: 616–20B, accuracy  $\pm 0.25\%$  full-scale (F.S)), with a range of  $\pm 10$  inches water column (in.w.c.)

were installed at a distance of 10 mm from the upper edge of the rectangular section of the each chamber. All instruments were connected to a personal computer via a signal conditioning unit for data acquisition. The vertical air velocity  $w$  ( $Q/A_2$ ) component through the orifice was measured at the centre of the orifice of each chamber by a hot wire anemometer with data collected with a real-time data logger (HHF-SD1) installed on the top of each chamber as illustrated in Fig. 3. These accurately read the data even at low air velocities. The incident wave energy was estimated using the wave characteristics measured via a wave gauge situated at the centre of the model position where the model was not in the tank (i.e., without having the MC-OWC in-situ).

### 3. Numerical model

#### 3.1. Numerical settings

##### Governing equations

The flow motion of an incompressible fluid can be described by the continuity equation (3), and momentum equation (4) of the Navier-Stokes equations (NS) [52]:

$$\nabla \cdot \bar{u} = 0 \quad (3)$$

$$\rho \left( \frac{\partial \bar{u}}{\partial t} + \bar{u} \nabla \bar{u} \right) = -\nabla \bar{p} + \mu \nabla^2 \bar{u} + \rho \cdot g_i - \rho \frac{\partial \tau_{ij}}{\partial x_j} \quad (4)$$

where  $i, j = 1, 2, 3$  for three-dimensional flows;  $\bar{u}$  is the fluid mean velocity field;  $\rho$  is the fluid density;  $\bar{p}$  is the fluid mean pressure field;  $g_i$  is  $i$ th component of the gravitational acceleration;  $\tau_{ij}$  is the Reynold stress tensor and  $t$  is time.

A CFD model with a computational three-dimensional domain (a numerical wave tank, or NWT) was constructed using STAR-CCM+ (a commercial numerical simulation package) to simulate the hydrodynamics and aerodynamics of a MC-OWC device. To simulate the flow motion of the incompressible fluid, the model solves the continuity and RANS equations. The free surface motion was modelled using the VOF method [53]. To enclose the equation systems, the Reynolds stresses were modelled using the two-equation shear stress transport (SST)  $k-\omega$  turbulence model. The Reynolds number ( $Re$ ) for the conditions tested was in the range of  $1 \times 10^6 < Re < 2.5 \times 10^6$ . To capture the boundary layer around OWC surfaces, ten prism layers with stretching factors of 1.5 and  $y$ -plus parameters of 1.0 were

utilized. These prism layers are important to capture the boundary layer developed on OWC chambers non-slip walls. These layers consist of a constructed mesh with the distance from the first mesh line to the non-slip wall called “ $y$ -plus” in non-dimensional form.

Fig. 4 illustrates the boundary conditions and detailed mesh views of the CFD model used in this study. The NWT had an overall length of ten wavelengths ( $L$ ) plus the length of the MC–OWC model. To reduce wave reflection on the right side of the NWT from the outlet boundary, a distance of one wavelength was assigned to the damping zone in front of the pressure outlet boundary. Within this zone, the vertical velocity component was modified by adding a resistance term to dampen the waves before approaching the outlet boundary [54]. Note that the absolute NWT length was not fixed for all the wave periods tested; instead, this length was adapted for each wave period to allow a total length of five wavelengths on the up-wave and down-wave sides of the MC–OWC device. This setup allows for the collecting of a reasonable amount of data (about eight wave cycles) before wave reflection from the OWC and interference from the outlet boundary with the incoming waves [55]. The height of the NWT was of 1.0 m that was equally split between the air and water phases. 3D CFD simulations are very expensive; therefore, it is beneficial to use symmetry planes when applicable. Using a symmetry plane in OWC devices was proved to have a negligible impact on device performance [56]. As a result, only half-width of the physical wave flume (0.45 m) was modelled in the NWT of this study with a symmetry plane as shown in Fig. 4(a). Since the ratio between the OWC breadth to the NWT width was 0.167 (i.e.,  $< 0.2$ ), the tank sidewall effects are expected to be nil as stated by Chakrabarti [38]. Regular wave velocity components were provided to the NWT on the left side through on the inlet boundary, whereas the top outlet boundary had the hydrostatic wave pressure assigned to it and the tank side and bottom boundaries were defined as slip walls. The free surface zone height was set to  $1.5 H$  (wave height  $H$ ). This was found to be sufficient and reduced the computation cost while still capturing the waves reflected by the OWC and minimising unwanted numerical wave height damping within the area of interest [56]. This height was further increased to  $2H$  inside each chamber (see Fig. 4 (c)) to capture any free surface amplification.

The computational domain mesh is crucial for confidence in the CFD results. STAR-CCM+ offers a user-friendly automatic meshing technique that was used in this study. The whole domain was initially meshed using a cell size of 400 mm and then reduced with more refinements using a trimmed cell mesher and a surface remesher. For the free surface refinement, the minimum number of cells were used; in the  $z$ -direction this was 16 cells per wave height and in the  $x$ -direction it was 74 cells per wavelength. These settings are very close to the recommendations given by ITTC [57] and CD-Adapco [58]. The cell aspect ratio (i.e., the ratio between the cell size in the longitudinal ( $\Delta x$ ) and vertical ( $\Delta z$ ) directions) was not allowed to exceed 16 [41]. Elhanafi et al. [56] recommended that the cell size  $\Delta y$  in the  $y$  direction (tank traverse) be set to 100 mm. The mesh refinement for the MC-OWC model was done using the mesh convergence study carried out by Elhanafi et al. [36] for a two-chamber 3D OWC. An OWC cell size of 6.25 mm was used (see Fig. 4 (d)), and the PTO surface was 0.781 mm (see Fig. 4 (e)). Note that it has been shown that these settings provide a good experimental agreement for an OWC device with one chamber [59-61]. The time step ( $\Delta t$ ) for each wave period ( $T$ ) was carefully selected, as recommended by CD-Adapco [58]; this was done to ensure the Courant number was always less than 0.5. A summary of the numerical settings and schemes used in this study can be found in Elhanafi et al. [56]

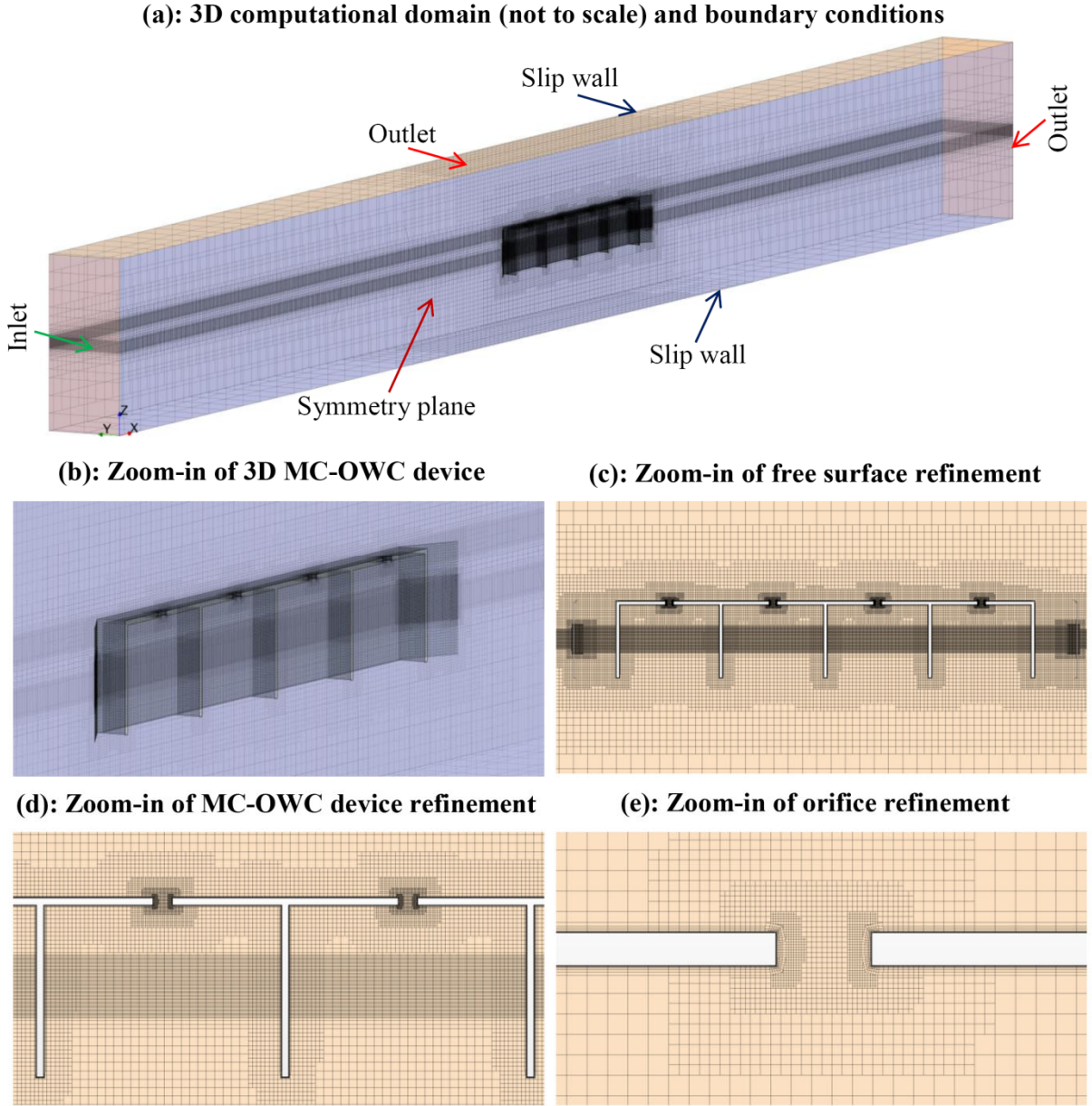


Fig. 4. Computational fluid domains

### 3.2. MC-OWC device performance

The differential air pressure ( $\Delta P$ ) was numerically monitored in each chamber by air pressure measurement at two points: the first is inside the chamber and the second is on the top outlet boundary domain. The airflow rate ( $Q$ ) was directly monitored by integrating the vertical air velocity over the entire area of the orifice. In each chamber, the free surface elevation ( $\eta$ ) was measured using virtual wave probes installed in similar locations to the physical model.

The power conversion capacity of the device is expressed by a fundamental quantity called a capture width ratio ( $\varepsilon$ ). This is defined as the mean power extracted by the device

divided by the incident wave mean power across the width of the device ( $b$ ). This ratio is given by

$$\varepsilon = \frac{P}{b \times P_{\text{in}}} \quad (5)$$

where  $P_{\text{in}}$  is the mean incident power per meter of the wavefront. This should not be confused with an efficiency factor because in some instances the device can extract energy from a wider field of wavefront so that this factor can be higher than one. Buoy devices in particular often do this. For regular waves,  $P_{\text{in}}$  is derived from Stokes second order wave theory [59] as given in

$$P_{\text{in}} = \frac{1}{16} \rho_w g H^2 \frac{\omega}{k} \left( 1 + \frac{2kh}{\sinh(2kh)} \right) \quad (6)$$

For a small OWC like the one tested here, air compressibility can be ignored. However, at full-scale, air compressibility can significantly affect the device performance, especially for a chamber of several metres in height [56, 62, 63]. Considering incompressible air, the pneumatic power that an OWC device can extract is expressed as [46]:

$$P = \frac{1}{T} \int_0^T Q(t) \cdot \Delta P dt \quad (7)$$

#### 4. Validation of the CFD model

One of the aims of this work is to validate the CFD model using experimental results of a complex hydrodynamic problem involving wave and MC–OWC interactions. Only one regular wave of height  $H = 0.087$  m and period  $T = 1.25$  s was used to verify the CFD model for the following performance parameters:  $\Delta P$ ,  $Q$  and,  $\eta$  with a constant PTO damping simulated with an orifice diameter  $D_2 = 36$  mm. The experimental results were limited but enabled the validation of the numerical models. The CFD and experimental time history results are compared in Fig. 5. In this figure, the experimental values of  $\Delta P$  values were not measured using the pressure transmitters due to large uncertainties associated with the sensors; instead,  $\Delta P$  was measured using the pre-calibration orifice approach (see Eq. (2)), which was proven to be valid [64].

It can be seen that the CFD results show good correlation with the experimental data. This agreement was quantified via the average correlation coefficient  $R$  and the Normalized Root Mean Square Error (NRMSE) given by

$$\text{NRMSE} = \frac{\sqrt{\frac{1}{N} \sum_{i=1}^N (x_i - y_i)^2}}{(X_{\max} - X_{\min})} \quad (8)$$

The average NRMSE and correlation coefficient  $R$  for all the validated parameters ( $\Delta P$ ,  $Q$ ,  $\eta$ ) are about 10 % and 0.89 as summarised in Table 1.

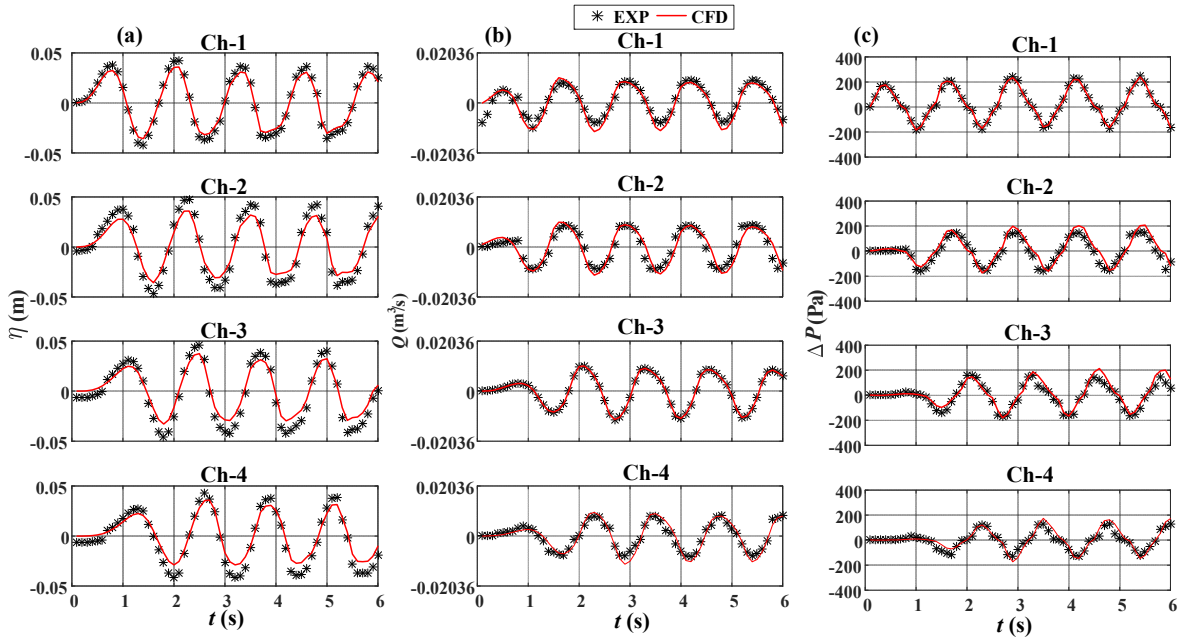


Fig. 5. Comparison experimental and CFD results for device performance parameters under a regular wave of height  $H = 0.087$  m, period  $T = 1.25$  s and orifice diameters  $D = 36$  mm. (a): water surface elevation ( $\eta$ ), (b): airflow rate ( $Q$ ) and (c): differential air pressure ( $\Delta P$ )

The good agreement achieved indicates the validity of the CFD model in simulating the behaviour of the MC–OWC device considered in this study. Therefore, the CFD model is utilised in the following sections to test the performance of the device under different wave conditions and various PTO damping coefficients.

Table 1. The correlation coefficient  $R$  and NRMSE between the CFD and the experimental results for chamber pressure ( $\Delta P$ ), airflow rate ( $Q$ ) and the free surface elevation ( $\eta$ )

Parameter		Ch-1	Ch-2	Ch-3	Ch-4	Average
$\Delta P$	NRMSE (%)	8.1	11.51	9.05	8.70	7.77
	$R$	0.99	0.83	0.88	0.87	0.89
$Q$	NRMSE (%)	10.05	12.03	0.61	7.87	7.64
	$R$	0.90	0.86	0.91	0.93	0.90
$\eta$	NRMSE (%)	5.48	11.37	11.69	11.54	10.00
	$R$	0.97	0.86	0.85	0.86	0.89

## 5. Results and discussion

### 5.1. Test conditions

After the numerical model was verified, the second set of tests was performed to study the effect on the performance of the MC–OWC of PTO damping. The verified CFD model was used to carry out numerous numerical simulations. In all, 96 simulations were carried out which comprised of six different PTO damping values simulated with different orifice diameters  $D$  (see Table 2) for two wave heights  $H = 0.045$  m (H1) and 0.087 m (H2) over eight wave periods as summarised in Table 3.

Table 2. Orifice diameter and its opening ratio

D(mm)	17	24	29.5	34	38	41.7
Ri (%)	R1 = 0.5	R2 = 1.0	R3 = 1.5	R4 = 2.0	R5 = 2.5	R6 = 3.0

Table 3. The period values used in CFD

$T$ (s)	0.8	1.0	1.12	1.2	1.3	1.6	1.8	2.0
Ti	T0	T1	T2	T3	T4	T5	T6	T7

### 5.2. Estimating device resonance

The resonant angular frequency ( $\omega_R = 2\pi/T_R$ ) of an OWC device can approximately be estimated by the expression given in [65]:

$$\omega_R = \sqrt{\frac{g}{d + 0.41\sqrt{A_1}}} \quad (9)$$

where  $d$  is the OWC device draught,  $A_1$  is the chamber waterplane area, and  $g$  is gravitational acceleration. For the device tested in this study, the estimated angular frequency was found

to be  $\omega_R = 6.67$  rad/s (the resonant period  $T_R \cong 0.94$  s). It is worth noting that this equation does not account for the pneumatic damping induced by the PTO system.

### 5.3. Effect of PTO damping on device performance

In this section, the CFD model was utilised to verify the validity of the quadratic relationship in Eq.(1) under a constant wave height H2 (0.087 m). It can be seen in Fig. 6 for a wave period T2 (1.12 s) that the relationship between  $Q$  and  $\Delta P$  follows a simple parabolic curve (the fitting curves are not shown in this figure) with a correlation coefficient  $R$  of not less than 0.9. The PTO damping coefficient ( $\tau$ ) was calculated using the instantaneous values of  $Q$  and  $\Delta P$  for each orifice tested as given in Eq. (1). The values of  $\tau$  were found to be in the range  $\tau_{\min} = 1036 \text{ kg}^{1/2} \text{ m}^{-7/2}$  at R6 to  $\tau_{\max} = 5200 \text{ kg}^{1/2} \text{ m}^{-7/2}$  at R1.

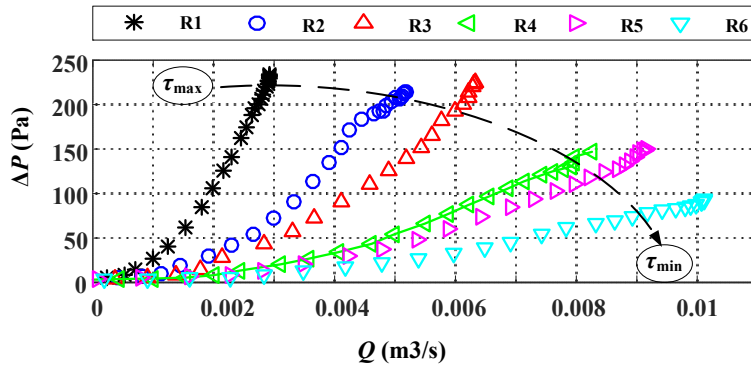


Fig. 6. The relation between the airflow rate ( $Q$ ) and the instantaneous differential air pressure ( $\Delta P$ ) for different PTO damping conditions simulated via various orifice opening ratio  $R_i$  (listed in Table 2)

The impact of the PTO damping has on  $Q$ ,  $\Delta P$  and  $\eta$  is illustrated in Fig. 7 at a constant wave condition ( $H_2, T_1$ ). Starting with the impact of the PTO damping coefficient ( $\tau$ ) on the free surface elevation ( $\eta$ ), Fig. 7 (a) shows that  $\eta$  decreased from more than 0.04 m to just above 0.01 m as  $\tau$  increases from  $1036$  to  $5200 \text{ kg}^{1/2} \text{ m}^{-7/2}$ . Furthermore, the first chamber (Ch-1) and the last chamber (Ch-4) experienced the highest and lowest free surface oscillations, respectively. Since the airflow rate ( $Q$ ) is related to the free surface vertical velocity ( $d\eta/dt$ ) (assuming incompressible flow), which can be calculated as the rate of change in the free surface elevation ( $\eta$ ) with respect to time (i.e.,  $d\eta/dt$ ), it was expected that the airflow rate follows the changes in  $\eta$  inside the chamber. This is shown in the results presented in Fig. 7 (b) where it is clear that  $Q$  in all chambers has the same trend of  $\eta$  with maximum and minimum values of about 0.01 and 0.0025 m<sup>3</sup>/s. These observations are in line with the results reported in [41, 66, 67] for a single chamber OWC device. With the relationship between  $\Delta P$  and  $Q$  shown in Fig. 6,  $\Delta P$  is seen in Fig. 7 (c) to gradually increase

from a minimum of 130 Pa to a maximum of 214 Pa with an increase in the damping coefficient. The pneumatic power ( $P$ ) is influenced by both  $\Delta P$  and  $Q$ ; hence, the results in Fig. 7 (d) illustrate that there is a maximum pneumatic power value at damping values of 1326 to 1500  $\text{kg}^{1/2} \text{ m}^{-7/2}$  at which point  $P$  peaks. The maximum pneumatic power was also found to decrease from 0.67 W in Ch-1 to 0.5 W in Ch-4.

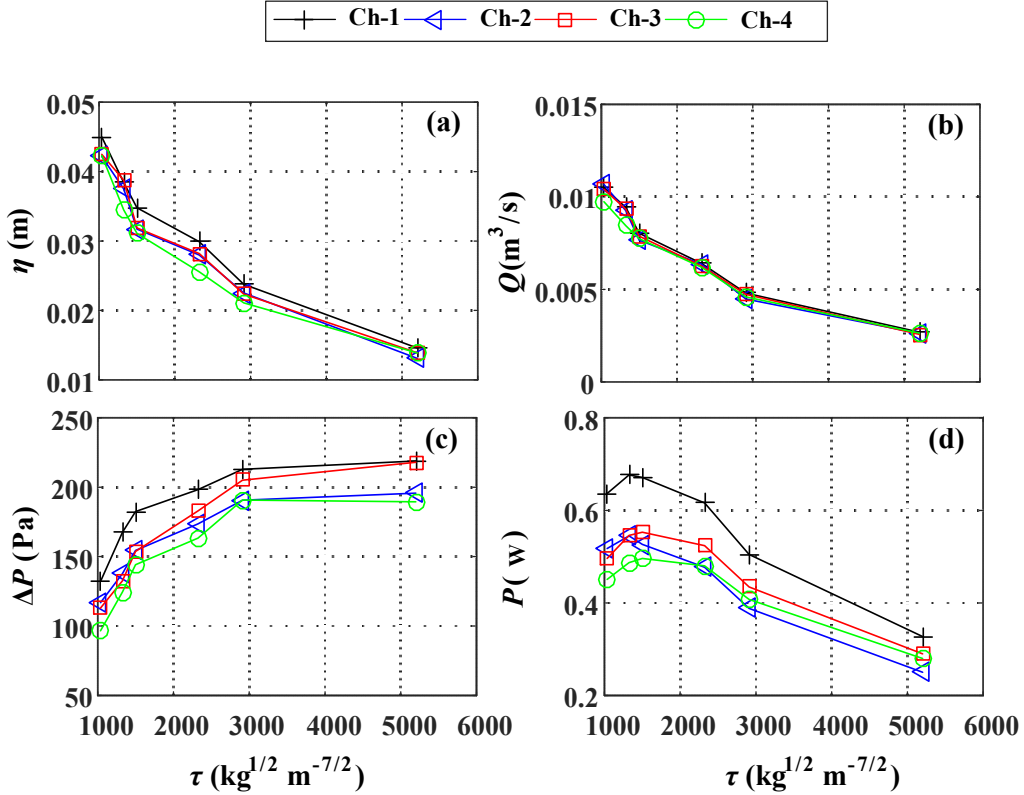


Fig. 7. Impact of PTO damping coefficient ( $\tau$ ) on the values of (a): the free surface elevation inside a chamber ( $\eta$ ), (b): the air volume velocity ( $Q$ ), (c): pressure change inside a chamber ( $\Delta P$ ) and (d): the pneumatic power ( $P$ )

One of the most important characteristics of a WEC device is the capture width ratio ( $\varepsilon$ ). The influence of the PTO damping on  $\varepsilon$  on each chamber of the MC–OWC studied here is shown in Fig. 8 for different wave periods (listed in Table 3). The results in this figure show a resonant period of 1.0 s (T1), which is very close to what was estimated from Eq. (9). For all chambers, the maximum capture width ratio was found at an optimum PTO damping value corresponding to R5, which indicates a negligible impact of chambers interaction on the selection of the PTO system for the whole device. The importance of the PTO damping in tuning the device to the incident wave condition is obvious for all chambers over the intermediate wave period range (T2–T6), where a lower PTO damping of orifice R3 provided a higher capture width ratio. Reduced damping of R1 could further improve the capture width ratio at the longest wave period tested.

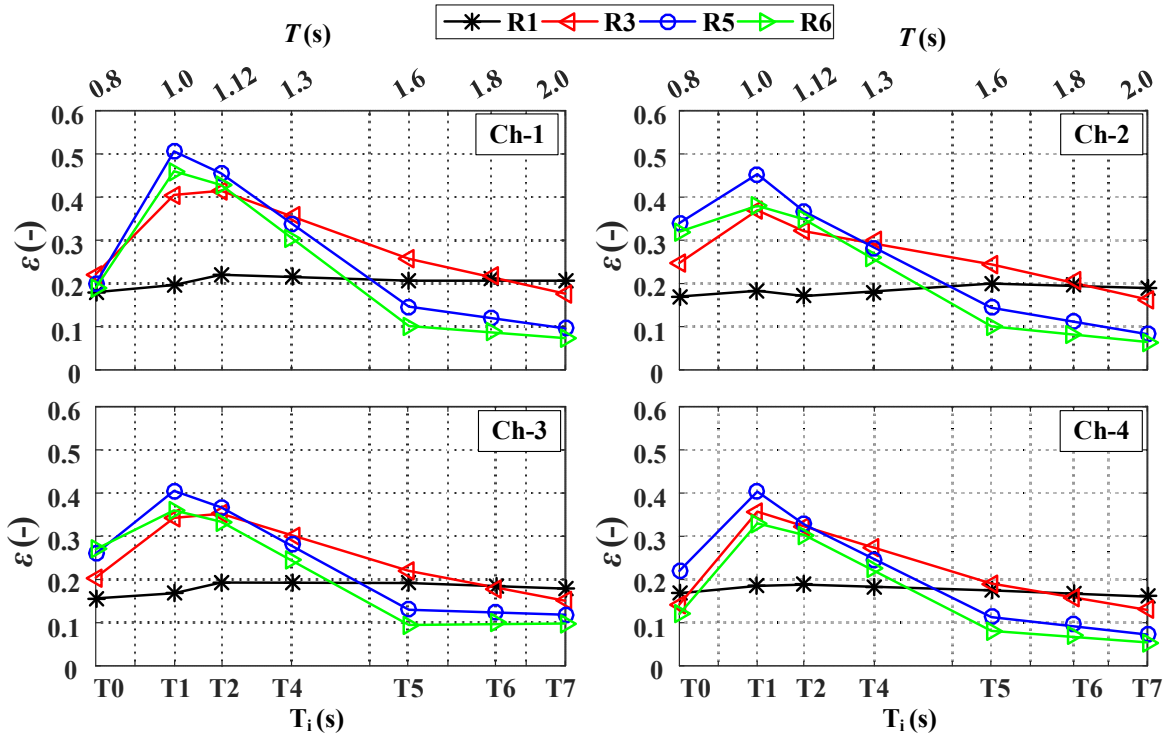


Fig. 8 Effect of PTO damping on the capture width ratio ( $\epsilon$ ) of each chamber for different wave periods and constant wave height ( $H_2 = 0.087$  m)

#### 5.4. Effect of wave height on device performance

The influence of the incident wave height on device performance is investigated in this section. This is done by decreasing the wave height to 0.045 m ( $H_1$ ). Fig. 9 demonstrates the effect the wave height has on the airflow rate ( $Q$ ), the free surface elevation ( $\eta$ ), the pressure difference ( $\Delta P$ ) and pneumatic power ( $P$ ) for range waves and with PTO damping using orifice opening ratio  $R_5$  (2.5 %). Both wave heights have almost identical general trends for all the parameters assessed. They decreased as wave height decreased from  $H_2$  to  $H_1$ . The wave height increase is almost 1.93 times (i.e., from 0.045 m to 0.087 m). Hence the incident wave power increased by about 3.74 times. However, the pneumatic power in all chambers increased on average by 3.56 times. This difference can be attributed to the slight increase and decrease in the reflected and transmitted energies respectively by the device resulting in reduced energy absorbed by the device [60].

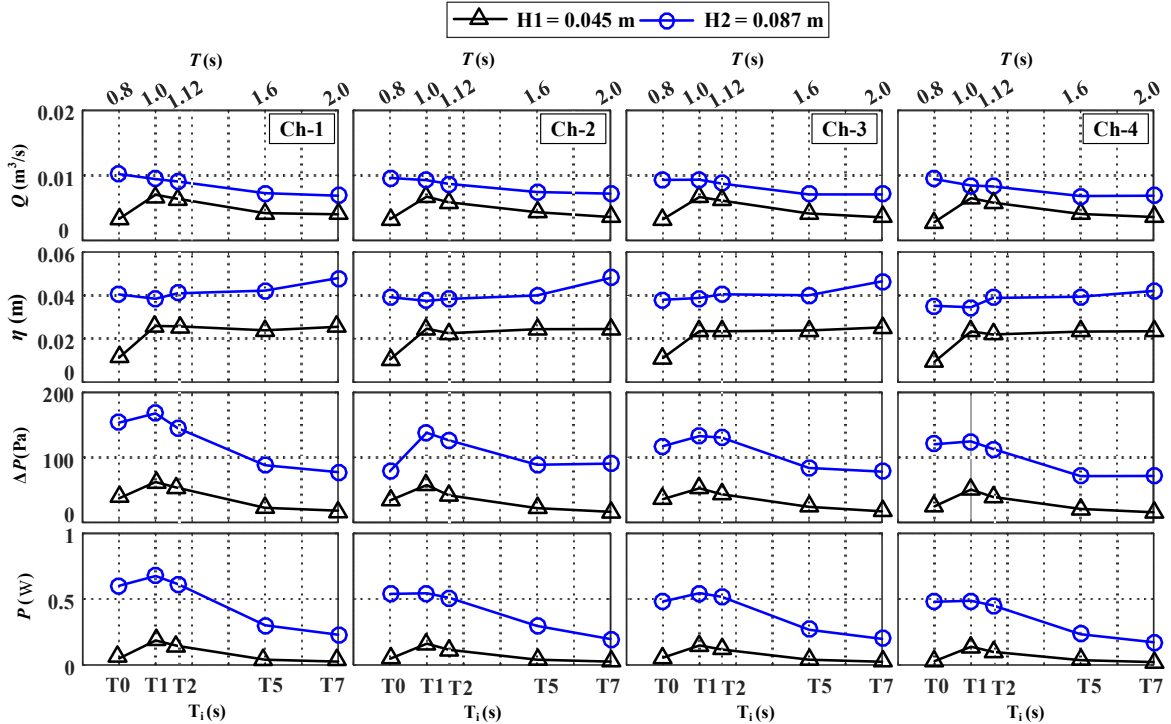


Fig. 9 Effect of wave height on airflow rate  $Q$  (1<sup>st</sup> row), the free surface elevation  $\eta$  (2<sup>nd</sup> row), differential air pressure  $\Delta P$  (3<sup>rd</sup> row) and the pneumatic power  $P$  (4<sup>th</sup> row) for different wave periods and a constant orifice opening ratio R5 (2.5%)

Fig. 10 illustrates the impact the wave height has on  $\varepsilon$  for each chamber. This is with a constant orifice opening ratio ( $R5 = 2.5\%$ ). The results demonstrate that all chambers have similar trends for  $\varepsilon$  under the two wave heights tested, such that  $\varepsilon$  initially increases with increasing wave period until a peak is reached at the resonant period (T1). Then it reduces with a further increase in the wave period. Under wave height H1 at T1,  $\varepsilon$  reaches a maximum value of 0.58, 0.50, 0.46 and 0.43 for in Ch-1, Ch-2, Ch-3 and Ch-4 respectively. These peak values reduced with increasing wave height (H2) to 0.50, 0.45, 0.41 and 0.40. A similar effect of wave height on single-chamber onshore and offshore OWC devices was previously reported [59, 61, 67, 68].

It is expected that, with increasing the incident wave height, not only the pneumatic power (see Fig. 9) but also the energy losses [60] increase. Furthermore, as mentioned earlier, changing the wave height affects the reflected and transmitted energies, which, in-turn, changes the amount of energy absorbed by the device structure. Elhanafi et al. [60] observed that the absorbed energy coefficient (i.e., the ratio between the absorbed energy and the incident wave energy) of an OWC device decreases with increasing the wave height, except for long wave periods where there was a noticeable increase in the absorbed energy coefficient. These observations help to understand the increase in  $\varepsilon$  shown in Fig. 10 only for wave periods longer than the resonant period.

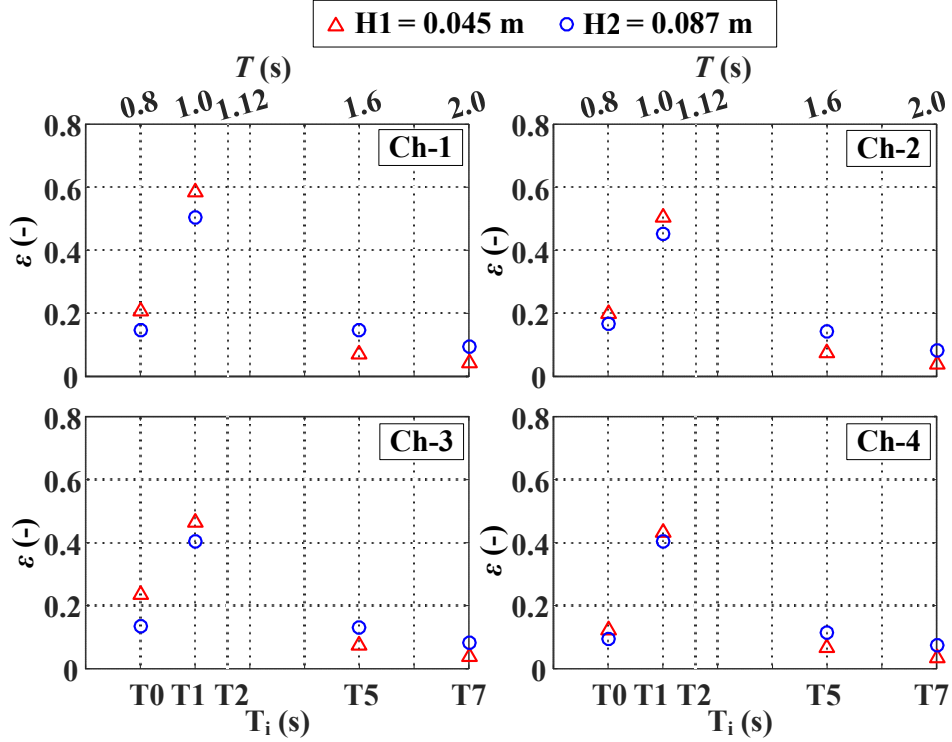


Fig. 10 Variation of the capture width ratio ( $\varepsilon$ ) of each chamber under different wave heights ( $H_1, H_2$ ), wave periods ( $T_0, T_1, T_2, T_5, T_7$ ) and a constant orifice opening ratio ( $R_5 = 2.5\%$ )

Similarly,  $\varepsilon_{\text{total}}$  ( $\sum_{i=1}^{i=4} P_i / (b \times P_{in})$ ), which is the overall capture width ratio for the MC–OWC, in Fig. 11 (a) shows that a maximum  $\varepsilon_{\text{total}}$  of 2.0 was achieved at a resonant period  $T_1$  (1.0 s) and  $H = 0.045$  m ( $H_1$ ), and that value reduced to 1.8 as the wave height increased to 0.087 m ( $H_2$ ) at the same resonant period. Overall, increasing the wave height from  $H_1$  to  $H_2$  improved  $\varepsilon_{\text{total}}$  by 1.2 to 2.2 times in the long-period range ( $T_i > T_2$ ), but it negatively impacted device performance in the short-period range ( $T_i < T_2$ ) resulting in a reduction of  $\varepsilon_{\text{total}}$  by 0.70 to 0.90 times. The effect of wave height on the PTO damping is shown in Fig. 11(b) at the device resonant period  $T_1$ . It can be seen that for all the tested PTO damping values, an increase in incident wave height reduces the maximum  $\varepsilon_{\text{total}}$ . The larger wave height  $H_2$  required a slightly larger orifice opening ratio (i.e., smaller PTO damping coefficient of  $\tau = 1036 \text{ kg}^{1/2} \text{ m}^{-7/2}$  at  $R_6$  instead of  $\tau = 1326 \text{ kg}^{1/2} \text{ m}^{-7/2}$  at  $R_5$ ). It is worth noting that these effects are in line with the experimental results reported in [59], which further support the applicability of the developed CFD model in studying the performance of such a complex MC–OWC device.

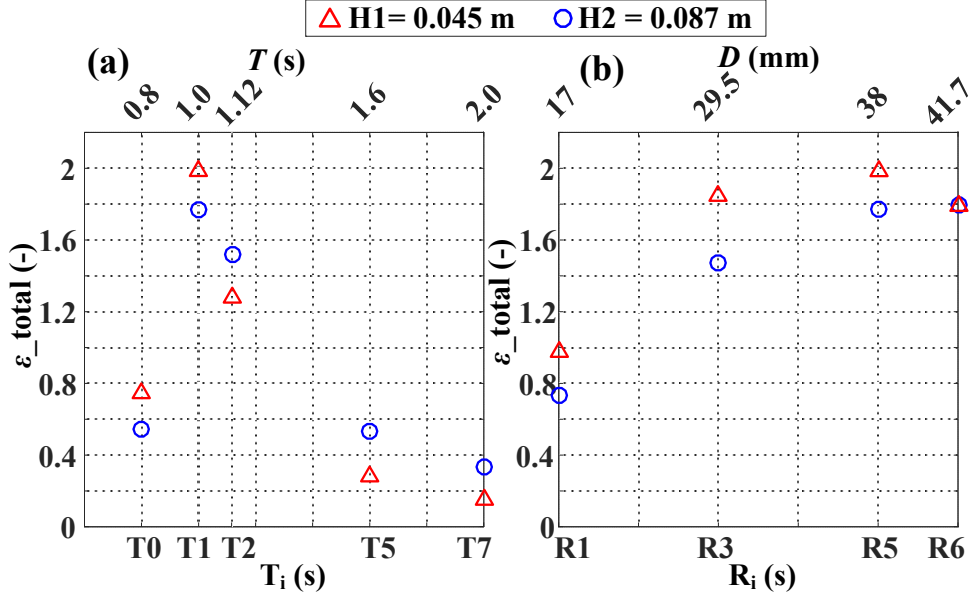


Fig. 11. Effect of wave height on total capture width ratio ( $\varepsilon_{\text{total}}$ ) for (a): different wave periods at constant opening ratio R5, (b): different opening ratios ( $R_i$ ) under resonant period T1

## 6. Conclusion

A 3D CFD model was constructed to simulate the behaviour of a MC–OWC device and to investigate the effect of PTO damping of device performance under different regular incident wave heights and periods. The CFD results show good agreement with the experimental measurements in all chambers for the following parameters: differential air pressure, chambers free surface elevation and airflow rate. The resonant period agreed very well with the value estimated from a commonly used formula.

It was found that increasing the PTO damping resulted in an increase in the differential air pressure and a decrease in both the free surface elevation and the airflow rate in all device chambers over the entire range of the wave periods tested. An intermediate PTO damping ( $\tau = 1326 \text{ kg}^{1/2} \text{m}^{-7/2}$ ) was found to maximise  $\varepsilon$  for all chambers overall wave periods, except for long waves, where a higher PTO damping was found to be more effective.

Increasing the wave height from 0.045 m to 0.087 m (i.e., 1.93 times) was found to significantly decrease the MC–OWC device total capture width ratio ( $\varepsilon_{\text{total}}$ ) for all PTO damping values tested by about 20 % in the short-period wave range, but  $\varepsilon_{\text{total}}$  showed an increase of about 76 % over the intermediate- and long-period wave ranges. The impact of changing the incident wave height on the resonant period was found to be negligible, but a larger wave height required slightly lower PTO damping.

The experimental tests performed in this work were limited and carried out in a small wave flume with a primary objective of initially validating MC–OWC mathematical and numerical models. Therefore, the next step in this project includes conducting further experimental tests under a wide range of regular and irregular wave conditions.

## References

- [1] Falnes J, A review of wave-energy extraction, *Marine Structures*; 20 (2007) 185-201.
- [2] Esteban M, Leary D, Current developments and future prospects of offshore wind and ocean energy, *Appl Energy*; 90 (2012) 128-36.
- [3] Magagna D, Uihlein A. JRC ocean energy status report.vol, Publications Office of the European Union: JRC93521;2015.
- [4] Delmonte N, Barater D, Giuliani F, Cova P, Buticchi G, Review of oscillating water column converters, *IEEE Trans on Industry Applications*; 52 (2016) 1698-710.
- [5] Clément A, McCullen P, Falcão A, Fiorentino A, Gardner F, Hammarlund K, et al., Wave energy in Europe: current status and perspectives, *Renewable and Sustainable Energy Reviews*; 6 (2002) 405-31.
- [6] Heller V, Development of wave devices from initial conception to commercial demonstration, *Comprehensive Renewable Energy*; 8 (2012) 79-110.
- [7] Chowdhury S, Nader J-R, Madrigal Sanchez A, Fleming A, Winship B, Illesinghe S, et al., A review of hydrodynamic investigations into arrays of ocean wave energy converters, retrieved February 2, 2016 from <http://arxiv.org/ftp/arxiv/papers/1508/150800866.pdf>; (2015).
- [8] Weber J. *WEC Technology Readiness and Performance Matrix—finding the best research technology development trajectory*. In: Proceedings of the International Conference on Ocean Energy, 17-19 October Dublin, Ireland 2012.
- [9] Folley M. Numerical Modelling of Wave Energy Converters: State-of-the-Art Techniques for Single Devices and Arrays London, UK: Academic Press; 2016
- [10] Khan N, Kalair A, Abas N, Haider A, Review of ocean tidal, wave and thermal energy technologies, *Renewable and Sustainable Energy Reviews*; 72 (2017) 590-604.
- [11] Falcão AF, Henriques JC, Oscillating-water-column wave energy converters and air turbines: A review, *Renew Energy*; (2015).
- [12] Falcão AdO. *The shoreline OWC wave power plant at the Azores*. In: Proceedings of the 4th European Wave Energy Conference, December 4-6 Aalborg, Denmark 2000.
- [13] Takahashi S, Nakada H, Ohneda H, Shikamori M. *Wave power conversion by a prototype wave power extracting caisson in Sakata port*. In: Proceedings of the 23rd International Conference on Coastal Engineering, October 4-9 Venice, Italy 1993.
- [14] Alcorn R, Hunter S, Signorelli C, Obeyesekera R, Finnigan T, Denniss T. Results of the testing of the Energetech wave energy plant at Port Kembla.vol Energetech Report;2005.
- [15] Washio Y, Osawa H, Nagata Y, Fujii F, Furuyama H, Fujita T. *The offshore floating type wave power device "Mighty Whale": open sea tests*. In: Proceedings of the Tenth International Offshore and Polar Engineering Conference, ISOPE, May 28 -June 2 Seattle, Washington, USA; 2000.

- [16] Uihlein A, Magagna D, Wave and tidal current energy–A review of the current state of research beyond technology, *Renewable and Sustainable Energy Reviews*; 58 (2016).
- [17] Fallon D, Hartnett M, Olbert A, Nash S, The effects of array configuration on the hydro-environmental impacts of tidal turbines, *Renew Energy*; 64 (2014) 10-25.
- [18] Shalby M, Dorrell DG, Walker P, Multi-chamber oscillating water column wave energy converters and air turbines: A review, *International Journal of Energy Research*; (2018).
- [19] Martinelli L, Pezzutto P, Ruol P, Experimentally Based Model to Size the Geometry of a New OWC Device, with Reference to the Mediterranean Sea Wave Environment, *Energies*; 6 (2013) 4696-720.
- [20] SEABREATH Ltd, Seabreath wave energy, <http://www.seabreath.it>; 2018 [Accessed 25 June 2018].
- [21] Rasmussen KD. The LEANCON Wave Energy Device, <http://www.leancon.com>; 2018 [Accessed 5 July 2018].
- [22] Kofoed JP, Frigaard P. Hydraulic evaluation of the LEANCON wave energy converter.vol Department of Civil Engineering, Aalborg University;2008.
- [23] Kelly T, Dooley T, Campbell J, Ringwood JV, Comparison of the Experimental and Numerical Results of Modelling a 32-Oscillating Water Column (OWC), V-Shaped Floating Wave Energy Converter, *Energies*; 6 (2013) 4045-77.
- [24] Arena F, Fiamma V, Laface V, Malara G, Romolo A, Viviano A, et al. *Installing U-OWC devices along Italian coasts*. In: Proceedings of the ASME 32nd International Conference on Ocean, Offshore and Arctic Engineering, June 9-14 Nantes, France; 2013.
- [25] Naty S, Viviano A, Foti E, Wave Energy Exploitation System Integrated in the Coastal Structure of a Mediterranean Port, *Sustainability*; 8 (2016) 1342.
- [26] Naty S, Viviano A, Foti E, Feaseability study of a wec integrated in the port of giardini naxos, italy, *Coastal Eng Proc*; 1 (2017) 22.
- [27] Vicinanza D, Contestabile P, Nørgaard JQH, Andersen TL, Innovative rubble mound breakwaters for overtopping wave energy conversion, *Coastal Eng* 88 (2014) 154-70.
- [28] Dorrell DG, Kazi S, Papadopoulos M. *Wave Generator Modelling using an Oscillating Water column and a Wells Turbine*. In: Proceedings of the Third IASTED International Conference on Power and Energy Systems, February 24-26 Palm Springs, USA 2003.
- [29] Dorrell DG, Halliday R, MacLean S, Miller P, Mosquera FS. *Development of Small-Scale Facilities for Initiating Studies into Sea Wave Energy generation*. In: Proceedings of the International Conference on Renewable Energy and power Quality, March 16-18 Zaragoza, Spain; 2005.
- [30] Dorrell DG, Halliday J, Miller P, Findlater M. *Review of wave energy resource and oscillating water column modelling*. In: Proceedings of the 39th International Universities Power Engineering Conference (UPEC) IEEE, September 6-8 Bristol, UK; 2004.
- [31] Hsieh M-F, Dorrell DG, Hsieh M-J, Lin C-C, Development of a wave energy converter using a two chamber oscillating water column, *IEEE Trans on Sustainable Energy*; 3 (2012) 482-97.
- [32] Shalby M, Walker P, Dorrell DG. *The Characteristics of the Small Segment Multi-Chamber Oscillating Water Column*. In: Proceedings of the 3rd Asian Wave and Tidal Energy Conferance, October 24-28 Singapore; 2016.

- [33] Shalby M, Walker P, Dorrell DG. *Modelling of the multi-chamber oscillating water column in regular waves at model scale*. In: Proceedings of the 4th International Conference of Energy and Environmental Research, Energy Procedia, July 17-20, Porto, Portugal; 2017.
- [34] Falcão AF, Henriques JC, Oscillating-water-column wave energy converters and air turbines: A review, Renewable Energy; 85 (2016) 1391-424.
- [35] Windt C, Davidson J, Ringwood JV, High-fidelity numerical modelling of ocean wave energy systems: A review of computational fluid dynamics-based numerical wave tanks, Renewable and Sustainable Energy Reviews; 93 (2018) 610-30.
- [36] Elhanafi A, Macfarlane G, Ning D, Hydrodynamic performance of single-chamber and dual-chamber offshore-stationary Oscillating Water Column devices using CFD, Appl Energy; 228 (2018) 82-96.
- [37] Rea M, Wave tank and wavemaker design, Ocean wave energy—current status and future perspectives, ed João Cruz, Springer-Verlag, Berlin Heidelberg, Germany; (2008) 147-59.
- [38] Chakrabarti SK. Offshore structure modeling: World Scientific; 1994
- [39] Cruz J. Ocean wave energy: current status and future perspectives: Springer Science & Business Media; 2007
- [40] Holmes B. Tank testing of wave energy conversion systems: marine renewable energy guides: European Marine Energy Centre; 2009
- [41] Elhanafi A, Fleming A, Macfarlane G, Leong Z, Numerical energy balance analysis for an onshore oscillating water column—wave energy converter, Energy; 116 (2016) 539-57.
- [42] He F, Huang Z, Hydrodynamic performance of pile-supported OWC-type structures as breakwaters: An experimental study, Ocean Eng 88 (2014) 618-26.
- [43] López I, Pereiras B, Castro F, Iglesias G, Performance of OWC wave energy converters: influence of turbine damping and tidal variability, International Journal of Energy Research; 39 (2015) 472-83.
- [44] Ning D, Wang R, Zhang C, Numerical Simulation of a Dual-Chamber Oscillating Water Column Wave Energy Converter, Sustainability; 9 (2017) 1599.
- [45] Crema I, Simonetti I, Cappietti L, Oumeraci H. *Laboratory experiments on oscillating water column wave energy converters integrated in a very large floating structure*. In: Proceedings of the 11th European Wave and Tidal Energy Conference (EWTEC), September 5-9 Southampton, UK; 2015.
- [46] Mendes A, Monteiro W. *Performance analysis of a model of OWC energy converter in non-linear waves*. In: Proceedings of the 7th European wave and tidal energy conference, September 11-13 Porto, Portugal; 2007.
- [47] Sarmento AJNA, Wave flume experiments on two-dimensional oscillating water column wave energy devices, Experiments in Fluids; 12 (1992) 286-92.
- [48] Pereiras B, López I, Castro F, Iglesias G, Non-dimensional analysis for matching an impulse turbine to an OWC (oscillating water column) with an optimum energy transfer, Energy; 87 (2015) 481-9.
- [49] Nielsen K. IEA ocean energy system Annex II Report.vol Ramboll, Denmark;2003.

- [50] López I, Pereiras B, Castro F, Iglesias G, Optimisation of turbine-induced damping for an OWC wave energy converter using a RANS–VOF numerical model, *Appl Energy*; 127 (2014) 105-14.
- [51] Simonetti I, Cappietti L, El Safti H, Oumeraci H. *Numerical modelling of fixed oscillating water column wave energy conversion devices: toward geometry hydraulic optimization*. In: Proceedings of the ASME 34th International Conference on Ocean, Offshore and Arctic Engineering, May 31-June 5 Newfoundland, Canada; 2015.
- [52] Wendt JF. Computational fluid dynamics: an introduction: Springer Science & Business Media; 2008
- [53] Hirt CW, Nichols BD, Volume of fluid (VOF) method for the dynamics of free boundaries, *Journal of computational physics*; 39 (1981) 201-25.
- [54] Choi J, Yoon SB, Numerical simulations using momentum source wave-maker applied to RANS equation model, *Coastal Engineering*; 56 (2009) 1043-60.
- [55] Elhanafi A, Fleming A, Macfarlane G, Leong Z, Numerical hydrodynamic analysis of an offshore stationary–floating oscillating water column–wave energy converter using CFD, *International Journal of Naval Architecture and Ocean Engineering*; 9 (2017) 77-99.
- [56] Elhanafi A, Macfarlane G, Fleming A, Leong Z, Scaling and air compressibility effects on a three-dimensional offshore stationary OWC wave energy converter, *Appl Energy*; 189 (2017) 1-20.
- [57] ITTC. Recommended Procedures and Guidelines: Practical Guidelines for Ship CFD Applications.vol, ITTC Report: 7.5-03 02-03;2011.
- [58] CD-Adapco. User Guid STAR-CCM+ Version 10.02.vol;2015.
- [59] Elhanafi A, Kim CJ, Experimental and numerical investigation on wave height and power take-off damping effects on the hydrodynamic performance of an offshore–stationary OWC wave energy converter, *Renew Energy*; 125 (2018) 518-28.
- [60] Elhanafi A, Macfarlane G, Fleming A, Leong Z, Experimental and numerical investigations on the intact and damage survivability of a floating–moored oscillating water column device, *Appl Ocean Research*; 68 (2017) 276-92.
- [61] Elhanafi A, Macfarlane G, Fleming A, Leong Z, Experimental and numerical investigations on the hydrodynamic performance of a floating–moored oscillating water column wave energy converter, *Appl Energy*; 205 (2017) 369-90.
- [62] Sarmento AJ, Falcão AdO, Wave generation by an oscillating surface-pressure and its application in wave-energy extraction, *Journal of Fluid Mechanics*; 150 (1985) 467-85.
- [63] Falcão AFO, Henriques JCC, Model-prototype similarity of oscillating-water-column wave energy converters, *International Journal of Marine Energy*; 6 (2014) 18-34.
- [64] Thiébaut F, Pascal R, Andreu A. *Investigation into the calibration of orifices used in OWC tank testing*. In: Proceedings of the 11th European Wave and Tidal Energy Conference (EWTEC), September 6-11 Nantes, France; 2015.
- [65] van't Veer R, Tholen HJ. *Added resistance of moonpools in calm water*. In: Proceedings of the ASME 2008 27th International Conference on Offshore Mechanics and Arctic Engineering, 15-20 June, The American Society of Mechanical Engineers (ASME), Estoril, Portugal; 2008.

- [66] Simonetti I, Cappietti L, Elsafti H, Oumeraci H, Optimization of the geometry and the turbine induced damping for fixed detached and asymmetric OWC devices: a numerical study, Energy; (2017).
- [67] Kamath A, Bihs H, Arntsen ØA, Numerical modeling of power take-off damping in an oscillating water column device, International Journal of Marine Energy; 10 (2015) 1-16.
- [68] Luo Y, Nader J-R, Cooper P, Zhu S-P, Nonlinear 2D analysis of the efficiency of fixed Oscillating Water Column wave energy converters, Renew Energy; 64 (2014) 255-65.